

# Cenozoic India-Asia collision driven by mantle dragging the cratonic root

Yanchong Li (✉ [yl79@illinois.edu](mailto:yl79@illinois.edu))

University of Illinois at Urbana-Champaign <https://orcid.org/0000-0002-9075-3887>

Lijun Liu

Institute of Geology and Geophysics, Chinese Academy of Sciences <https://orcid.org/0000-0002-3232-0151>

Diandian Peng

University of California San Diego <https://orcid.org/0000-0002-8664-2164>

Zebin Cao

University of Illinois at Urbana-Champaign <https://orcid.org/0000-0001-9899-2965>



---

## Article

### Keywords:

**Posted Date:** November 21st, 2023

**DOI:** <https://doi.org/10.21203/rs.3.rs-3460307/v1>

**License:**   This work is licensed under a Creative Commons Attribution 4.0 International License.  
[Read Full License](#)

**Additional Declarations:** There is **NO** Competing Interest.

---

# Abstract

The driving force behind the Cenozoic Indian-Asia collision remains elusive. Using global-scale geodynamic modeling, we find that the continuous motion of the Indian plate is driven by a prominent upper-mantle flow pushing the thick Indian lithospheric root, originated from the northward rollover of the detached Neo-Tethyan slab and sinking slabs below East Asia. The maximum mantle drag occurs within the strong Indian lithosphere and is comparable in magnitude to that of slab pull ( $10^{13}$  N/m). The thick cratonic root enhances both lithosphere-asthenosphere coupling and upper-plate compressional stress, thereby sustaining the topography of Tibetan Plateau. We show that the calculated resistant force from the India-Asia plate boundary is also close to that due to the gravitational potential energy of Tibetan Plateau. Our findings suggest that this mantle flow is key for the formation of the Tibetan Plateau and represents part of a hemispheric convergent flow pattern centered on central Asia.

## Main Text

The continuous northward convergence of the Indian plate with Tibet after their Cenozoic ( $\sim 50$  Ma) collision<sup>1,2</sup> (Fig. 1, Movie S1) represents a key linkage among the termination of the Neo-Tethyan ocean, the birth of the Indian Ocean, and the formation of Tibetan Plateau. However, the driving force of this unique Cenozoic plate kinematics remains an intriguing outstanding question<sup>3</sup>. In addition, geophysical analysis suggests that the late-Cenozoic resistance force due to the gravitational potential energy (GPE) of the Himalayas and Tibetan Plateau ranges from  $3 \times 10^{12}$  N/m to  $8 \times 10^{12}$  N/m<sup>4-6</sup>. Consequently, the northward driving force should be only higher than this value given the potential resistance from other boundaries of the Indian plate<sup>7</sup>. Yet, slab pull, the most commonly invoked plate driving force with a comparable amplitude ( $10^{13}$  N/m)<sup>8</sup>, is largely negligible because of the absence of a continuous oceanic slab below the present collision zone<sup>9,10</sup>. Ridge push, on the other hand, is too small, given its typical amplitude of  $3 \times 10^{12}$  N/m<sup>5,6,8</sup>. Thus, the post-collisional Indian motion cannot be explained by the classic plate driving forces<sup>7</sup>.

This problem has invoked multiple hypotheses. One of these refers to the continuous subduction of the continental lithosphere which is considered dense enough to provide an alternative slab pull force<sup>13,14</sup>. However, their predicted depth-continuous steep slab is at odds with the observed seismic structure where the Indian lithosphere is shallowly underplating Eurasia with no connection to prominent deeper slabs<sup>9,10,15,16</sup>. Another proposal suggests that nearby subducting plates like the Capricorn and Australian plate transmit far-field slab pull from below Southeast Asia to the Indian plate interior<sup>3,6,17-19</sup>, but this mechanism is dynamically challenging for neighboring plates with near-parallel motion directions<sup>20</sup>, and the situation is even worse with the additional need to overcome the large GPE-induced resistance from Tibet.

A conceptually more feasible driving force is the mantle drag from the faster-moving asthenosphere acting at the bottom of the lithosphere<sup>21-23</sup>, where the associated fast mantle flow was proposed to be

induced either by a rising plume<sup>23</sup> and/or suction of foundered slabs<sup>22</sup>. However, many aspects of this driving force remain unclear, such as its amplitude and duration, how the asthenosphere interacts with the lithosphere, the physical origin of the fast mantle flow, and its capability in maintaining both plate motion and India-Tibet collision. We suggest that answering these questions requires a more systematic and quantitative analysis of the entire dynamic system.

## Results

### Cenozoic slab evolution and mantle flow

We tackle these problems using a global, sequential-in-time data-assimilation model starting from 200 Ma (see Method for more details) based on a recent plate reconstruction (2). This model generates evolving mantle structures (Fig. S1) including slabs and large-low-shear-velocity provinces (LLSVPs) that match present-day tomographic structures both regionally (Fig. 3a) and globally<sup>24-27</sup>. Its temporally evolving continental lithospheric thickness in response to mantle dynamics also allows quantifying the lithosphere-asthenosphere interaction due to the variable LAB (lithosphere-asthenosphere boundary) depth (Fig. 3c, S1c, d), as recently done<sup>28,29</sup>. To reproduce observed plate motion at different times using a fully dynamic approach, we solve the flow using the corresponding mantle structures from the data-assimilation model while allowing the surface to deform freely in the horizontal directions. During this calculation, we also vary the effective viscosity values of the plate boundaries and the oceanic asthenosphere, both of which are not well determined during the initial sequential simulation. After obtaining a satisfactory match between modeled and observed plate motion at the present, the same viscosity adjustment is applied to all other times (Method). Finally, based on these results we analyze the properties and origin of the relevant forces.

Our model's reproduction of present-day global plate motion (Fig. 2a) is comparable to, or better than published results<sup>17,22,30</sup>. As a step further, our calculation also properly reproduces the past motions of the Indian plate (Fig. 2b, c, 4c). A prominent dynamic feature is that the asthenospheric flow south of the Indian continent is consistently much faster than the surface plate motion. The good fit between modeled (Method) and observed asthenospheric (200 km depth) seismic anisotropy (Fig. 2d) further validates the existence of this fast mantle flow. These results indicate that the previously hard-to-quantify viscous mantle drag should act as an important driving force for the persistent Cenozoic Indian plate motion.

In our model, the faster-than-surface asthenospheric flow is a direct result of the lateral dynamic pressure gradient in the upper mantle, where the pressure is high beneath the southern Indian Ocean and low beneath the Indian continent (Fig. 3b). This pressure gradient exerts a net force pushing the mantle to go northward, generating a type of flow called the Poiseuille flow<sup>26</sup>. Consequently, the overriding Indian lithosphere, which moves more slowly due to resistance from its boundaries, especially on the northern side, experiences a mantle drag from the fast-moving asthenosphere below it.

The low-pressure upper mantle beneath the Indian continent is a combined result of 1) the sinking and southward rollover of the Neo-Tethyan slab in the mid-lower mantle, and 2) the voluminous slab pile beneath Eurasia at lowermost mantle depths comprising both the Neo-Tethyan and Izanagi slabs<sup>24</sup>. The southward rollover of the sinking Neo-Tethyan slab at lower-mantle depth, caused by continuous trench advance, reduces the pressure beneath the subducting plate instead of the overriding plate, with the latter being more commonly observed with retreating slabs. The relatively high pressure in the upper mantle south of the continent is partly due to the upwelling plume from the underlying African LLSVP. Both the subducted slabs and upwelling plumes are consistent with seismic tomography (Fig. 3a).

The amplitude of dynamic pressure and its lateral gradient scale linearly with the density anomalies and only weakly depend on mantle viscosity, for a given spatial pattern of mass distribution<sup>32</sup>. This property allows us to estimate the relative contributions of various density anomalies to the observed present-day plate motion and associated mantle drag, without worrying about the effect of mantle viscosity. Compared to the Eurasian slab pile, the Neo-Tethyan slab is less voluminous, thus its removal only slows the Indian plate by  $\sim 20\%$  (Fig. S2c, S3b). However, in this case, the Eurasian plate moves northward much faster at a similar rate to India, implying little convergence between the two plates. Removing lower mantle slabs globally will stop the mantle flow and its driving of the Indian plate (Fig. S2f, S3c), consistent with the scenario where both slab pull and slab suction are absent<sup>22</sup>. Thus, both slab piles are essential in driving Indian convergence: while the voluminous Eurasian slab pile generates regional-scale low pressure below central-eastern Asia, the Neo-Tethyan slab interjects to expand the low-pressure center to below north India and generate the proper asthenosphere flow pattern associated with the observed India-Tibet convergence (Fig. 3b). This highlights a complex multiscale interaction among the sinking mantle slabs that is hard to illustrate in simpler models used previously.

As a further step from earlier studies, the time-dependent nature of our model allows us to examine the evolution of the slab and its control on the mantle flow during the geological past. The detachment of the Neo-Tethyan slab happened between 50 Ma and 40 Ma after the closure of the Neo-Tethyan ocean (Fig. 3d, e). In contrast to the traditional slab suction hypothesis<sup>22,33</sup>, the faster-than-surface upper-mantle flow appeared even before the slab detachment (Fig. 3d). This flow was likely attracted by the Izanagi subduction in the north, which also induced the Neo-Tethyan trench advance and slab rollover. This fast asthenospheric flow lasts from  $> 50\text{Ma}$  to the present day, thus representing the primary force driving the Indian plate throughout the post-collision Cenozoic history.

## **Mantle drag due to lithosphere-asthenosphere interaction**

While some previous research suggested mantle flow as a potential driving mechanism for the post-collisional Indian motion<sup>23,34</sup>, the existence, magnitude, distribution, and evolution of this force all remain unclear. For example, the much lower (by many orders of magnitude) asthenospheric viscosity than that of the overlying lithosphere seems to dismiss mantle drag as a major driving force<sup>35,36</sup>. Thicker lithospheric keels could affect the coupling between the lithosphere and the underlying mantle, but this effect on continental motion is uncertain<sup>7,36,37</sup>, due to its strong dependence on the poorly constrained

mantle flow pattern. Therefore, it is necessary to further quantify the flow-induced mantle drag and how the asthenosphere interacts with the lithosphere with the presence of a weak asthenosphere and variable LAB depth in an evolutionary model.

Mantle drag consists of two types (Fig. 4a, b): 1) Friction drag due to shear stress along the lithosphere boundary, and 2) pressure drag due to force normal to the contact surface through pressure gradients. Inside the convecting Earth, friction drag originates from the vertical gradient of horizontal flow within the bottom of the lithosphere, while pressure drag mostly occurs along lithospheric steps where the LAB depth varies laterally. Our analysis (Method) shows that the magnitude of total mantle drag along the plate motion direction is  $1.1 \times 10^{13}$  N/m at present, exceeding the highest estimation ( $8 \times 10^{12}$  N/m) of Tibetan resistance from the northern plate boundary. Among this force, friction drag has a dominant magnitude of  $8.8 \times 10^{12}$  N/m while pressure drag is  $2.2 \times 10^{12}$  N/m (Fig. 4a, b).

Interestingly, both friction drag and pressure drag show a prominent concentration around the southwestern edge of the Indian continent, where a large lithospheric step exists. This concentration accounts for  $\sim 50\%$  of the total friction drag and nearly 100% of the pressure drag. Spatially, this lithospheric step corresponds to a sharp slowdown of the asthenospheric flow that is blocked by the thicker continental keel to the northeast (Fig. 2b). This observation confirms the important role of a thicker lithospheric root for increasing coupling between the plate and the asthenosphere<sup>29,36</sup>.

The resistant force acting on the northern plate boundary ranges from  $3.8 \times 10^{12}$  N/m to  $9.7 \times 10^{12}$  N/m during the past 30 Ma (Fig. 4b, c), comparable to the total mantle drag as well as the GPE estimation ( $3 \times 10^{12}$  N/m to  $8 \times 10^{12}$  N/m)<sup>4-6</sup>. This means that most of the driving force is balanced by the collisional resistance from the India-Asia collision. The largest resistant force is located in the mid-western part of the collision zone, likely as a direct reaction along the plate motion direction to the large driving force from the southwestern edge of Indian continent. This shows that our model, although not explicitly including a free-surface to mimic the high plateau topography, captures the correct sub-surface vertical stress along the plate boundary that represents the correct GPE as occurred in reality.

In contrast to the traditional view that a weak asthenosphere diminishes the mantle drag (35, 36), our results demonstrate that the maximum frictional stress occurs within the relatively strong lithospheric root (Fig. S4a). Inside the weak asthenosphere, the maximum friction drag is about half of that within the lithosphere above (Fig. S4b, c), much greater than that implied from a linear proportion scaled with viscosity, as previously found (36). In general, the effective mantle drag gradually increases from the weak asthenosphere to the strong lithospheric interior, irrespective of their viscosity contrast.

However, reducing the asthenospheric viscosity does help decouple the plate from the underlying mantle. A set of models with uniform lithospheric thickness but varying asthenospheric viscosity confirm this effect (Fig. S5), where the mantle drag decreases by a factor of 2.5 (from  $5 \times 10^{12}$  N/m to  $2 \times 10^{12}$  N/m) as asthenospheric viscosity drops by a factor of 20 (from  $1 \times 10^{20}$  Pa·s to  $5 \times 10^{18}$  Pa·s), consistently below the level of resistance force due to Tibetan GPE. On the other hand, further increasing the asthenospheric

viscosity will lead to a saturation in the magnitude of mantle drag (see the relative change in asthenospheric viscosity and mantle drag in Fig. S5). This result further confirms the previous finding that, for a given density distribution, buoyancy has a much stronger control on sub-lithospheric stress than mantle viscosity<sup>32</sup>. Consequently, lithospheric thickness variation must contribute additionally to balance the resistance from the Tibetan Plateau.

Previous studies adopting a uniform lithospheric thickness were able to reproduce the present Indian motion<sup>23</sup>, thus raising a question on the respective roles of friction drag, pressure drag, and Tibetan resistance. To explore these forces and the resulting plate motion predictions, we successively reduce the thickness of the continental root. This reduction leads to progressively smaller mantle drags (Fig. S6a-c) that eventually fall below the threshold of Tibetan resistance ( $3 \times 10^{12}$  N/m, (5)). With the maximum root depth being 200 km (250 km in the reference case), the Indian plate motion decreases slightly due to a smaller drag of  $8.4 \times 10^{12}$  N/m (Fig. S6a). However, truncating the root below 175 km leads to an increase in plate velocity although the drag is even smaller ( $6.8 \times 10^{12}$  N/m; Fig. S6b). This increase of velocity may be attributed to the greater reduction in plate boundary resistance than in mantle drag. If the Indian plate is of a uniform thickness of 100 km (as in (23)), while the predicted plate motion remains acceptable, the mantle drag falls below the lowest estimate of Tibetan resistance ( $2.1 \times 10^{12}$  N/m compared to  $3 \times 10^{12}$  N/m; Fig. S6c). These results further suggest that the continental root affects the transmission of mantle drag into the overlying lithospheres in two ways: 1) to couple the Indian plate with the underlying asthenosphere, and 2) to maintain a large contact area between Indian and Eurasian plates. Thus, the continental root strongly modulates the balance among the mantle drag, the Indian plate motion, and the northern boundary resistance from the Tibetan Plateau. A recent study shows that the craton is compressed by mantle convection<sup>38</sup>, which is similar to our study except that one side of the cratonic India is sustained by continental collision. Since the mantle drags concentrate on the root edge that faces the fast mantle flow, the exact geometry of the root will unlikely affect the overall coupling as long as the flow-normal area of the edge remains similar.

While some researchers suggest that the upwelling plume has a strong impact on mantle drag in this region<sup>23</sup>, our model reveals that the plume arises from the boundary of the African LLSVP (Fig. 3f) does not significantly affect dynamic pressure beneath the Indian plate (Fig. 3b). To further examine the effect of mantle upwelling, we perform a test by removing all hot mantle anomalies in the model. Surprisingly, the reproduced Indian plate motion remains similar, and so does the amount of mantle drag (Fig. S7). In addition, a recent seismic tomography study shows that the plume is mainly located beneath the Somalian plate, indicating its limited contribution to driving the Indian plate<sup>39</sup>. Therefore, we suggest that sinking slabs play a more crucial role than rising plumes in driving the Indian plate motion.

Following the same model setup that generates the preferred present-day forces (Fig. 4a, b) and kinematics (Fig. 2), we extend the analysis to the geologic past. The calculated mantle drag is consistently larger than the present-day value ( $\sim 10^{13}$  N/m), with that at 50 Ma being twice as large (Fig. 4c). The calculated drag history closely follows the temporal trends of both predicted and observed

plate motions since  $\sim 45$  Ma (Fig. 4c) when India-Tibet collision started in the model (Fig. 1), further confirming mantle drag as the dominant driving force. Our estimated plate motion cannot reproduce the much faster observed Indian motion from 60 Ma to 50 Ma. Both the small magnitude of mantle drag and the assumed single subducting slab (Fig. 3d) during this period implies the operation of other potential driving forces such as those discussed below.

## Implications on forces driving plate motion and continental collision

The quantification of the Cenozoic mantle drag permits a reevaluation of other potential plate-driving forces. Although our model assimilates lateral density variations of oceanic lithosphere following seafloor age, it likely does not fully capture the effect of ridge push due to the flat model surface across the spreading center. However, given its small magnitude of  $\sim 3 \times 10^{12}$  N/m<sup>8</sup> that cannot even overcome the minimum estimate in Tibetan GPE force<sup>5</sup>, ridge push is unlikely to be a major driving force for the Cenozoic Indian motion. We suggest this should be a secondary force that might contribute to explaining the slightly slower predicted plate motion compared to observation (Fig. 4c).

Additional results reveal that slab pull from nearby subduction<sup>3</sup>, specifically the Sumatra-Java slab pull (Fig. S8) acting through the Indian-Capricorn plate (IND-CAP) boundary (Fig. 1a), should also be minor compared to mantle drag. In practice, the Indian mantle drag and the IND-CAP boundary drag are complementary forces in driving Indian plate motion. With weakened Indian plate boundaries (to minimize surrounding forces), a uniformly thick Indian lithosphere, and a weak asthenosphere (to minimize mantle drag), the Indian plate experiences nearly no motion (Fig. S6d). Strengthening the IND-CAP boundary based on this model (Fig. S6f) to allow the transmission of the Sumatra slab pull to India only produces a small fraction of the observed plate motion, similar to the scenario where the Indian continental root is thickened by 50 km to increase the lithosphere-asthenosphere coupling (Fig. S6e). Since these two models predict similar plate motion, the extra  $1 \times 10^{12}$  N/m mantle drag in the latter model could approximate the amount of IND-CAP boundary drag in the former model, thus confirming its minor role in sustaining the Cenozoic Indian-Tibetan collision.

Our model does not reproduce the faster plate motion ( $> 10$  cm/yr) observed before  $\sim 50$  Ma. This implies the existence of other driving forces besides mantle drag. Relevant hypotheses include a rising plume head<sup>40,41</sup>, additional slab pull due to double subduction<sup>42</sup> and thinning of Indian lithosphere<sup>43</sup>. Our model does not produce a major plume around this time (Fig. 3d-f), thus not capturing this additional force. The plate reconstruction we adopted does not consider a double subduction scenario either - it instead incorporates a back-arc setting with a southward trench jump<sup>2</sup>. Model tests also show the reduction of lithospheric thickness can increase plate speed with small driving force (Fig. S6b). Therefore, we propose that these alternative hypotheses were likely at play during the earliest Cenozoic.

The history of the India-Tibet collision provides additional support for the underlying mantle drag as the dominant driving force. The estimated present-day southward resisting force from the Tibetan Plateau

$(3 \times 10^{12} \text{ N/m to } 8 \times 10^{12} \text{ N/m})^{4-6}$  matches our estimated resistant force from the northern boundary since 30Ma. It also provides a minimum estimate of the required amount of northward Indian plate driving force, substantiating the necessity of mantle drag acted on a thick continental root, since the amplitude of the mantle drag is notably larger than that of other relevant forces as discussed above. The India-Tibet collision history was characterized by persistent northward advancement of the Neo-Tethyan subduction zone, which likely started in the Cretaceous when India initially rifted off from Gondwana<sup>43</sup>. This phenomenon is unique among global plate tectonics where most oceanic trenches tend to roll back. Our results show that a strong northward mantle drag existed even before the onset of collision (e.g., 50 Ma, Fig. 1c). This drag not only maintains the Indian motion but also carry the trench northward, which is a dynamic feature that has not been addressed in most previous studies.

## Discussion

What sets our findings apart from previous studies is the identification of a plate-scale convection cell spanning the entire mantle depth below India. This convection cell is part of a broader hemispheric convergent flow pattern at the upper-middle mantle depth centered primarily below Tibet (Fig. 5, Movie S2). The trajectory of the subducting Neo-Tethyan slab outlines the larger-scale flow structure at its southern edge, with upper-mantle northward and lower-mantle southward motion. This unique flow pattern is mostly independent of the detailed tectonic setting between the Indian Plate and the Tibetan Plateau during their collision, but instead controlled by the long-term (since the early Mesozoic) subduction history within the eastern hemisphere, where the Tethyan, Paleo-Pacific, and Paleo-Mongolian Plates have subducted beneath Eurasia from the south, east, and north, respectively<sup>2</sup>.

Recently, we showed that this multi-slab dynamic system progressively decreased the dynamic pressure below East Asia during the late Mesozoic, firstly leading to the formation of a Late-Cretaceous continental-scale flat Izanagi slab<sup>25</sup>, and subsequently forming the stagnant slabs below East Asia<sup>26</sup>. Further south and east around the East Asian margins, the same flow regime may also explain the rapid northward motion of the Australian plate<sup>2</sup>, as well as the formation of back-arc basins along the entire west Pacific margin<sup>28</sup>, all occurring in the Cenozoic. This dynamic effect is also similar to that driving the westward motion of North America<sup>45</sup>.

Therefore, the Cenozoic India-Tibet collision is just one of the multiple tectonic expressions of this hemispheric convergence flow pattern. Unlike other circum-Asia regions where the abutting tectonic plates are wide, the Neo-Tethyan-Indian plate is narrow in the east-west direction bounded by transform faults and mid-ocean ridges (Movie S1). Its unique geometry and location above the conjunction of the Tethyan-Pacific subduction zones allow it to respond more readily to the underlying mantle drag. This property shapes the unique northward Indian kinematic history, the special rollover geometry of the Neo-Tethyan slab, and the resulting persistent continent-continent collision forming the Tibet Plateau. We propose that this long-lasting hemispheric convergence should represent an important driving force for the one-way tectonic train closing the Tethyan belt<sup>46</sup>, and may also eventually lead to the formation of



the next supercontinent around Eurasia<sup>47</sup> by transforming the current degree-2 global mantle flow pattern to a degree-1 configuration<sup>48</sup>.

## Methods

### Governing Equations and Data assimilation

The global spherical geodynamic model is based on the code CitcomS<sup>49</sup>. The mantle is divided into 12 caps, each with a high-resolution mesh consisting of 257 x 257 x 113 nodes, equivalent to a horizontal (vertical) resolution of 25 km (12 km) near the surface. This resolution allows a proper capture of the lithospheric structure, especially its interaction with the convective mantle. We assume the mantle is incompressible and satisfies the Boussinesq approximation. The model simulates subduction history and mantle evolution through the last 200 Myr. The conservation equations for mass, momentum, energy, and chemical particles are:

$$\nabla \cdot \vec{u} = 0 \# (1)$$

$$-\nabla P + \nabla \cdot \left[ \eta \left( \nabla \vec{u} + \nabla^T \vec{u} \right) \right] + (\rho_m \alpha \Delta T + \Delta \rho_c) \vec{g} = 0 \# (2)$$

$$\frac{\partial T}{\partial t} + \vec{u} \cdot \nabla T = \kappa \Delta T \# (3)$$

$$\frac{\partial C}{\partial t} + \vec{u} \cdot \nabla C = 0 \# (4)$$

where  $\vec{u}$  is velocity,  $P$  is dynamic pressure,  $\mu$  is viscosity,  $\rho_m$  is the density of the ambient mantle,  $\Delta \rho_c$  is the compositional density anomaly,  $\vec{g}$  is the gravitational acceleration,  $T$  is temperature,  $\kappa$  is the thermal conductivity,  $C$  is chemical composition.

To reproduce natural, tabular, and asymmetrically subducting slabs that move freely and satisfy observed plate kinematics, we utilize a data-assimilation technique<sup>50-52</sup> that incorporates a recent plate reconstruction model<sup>2</sup>. The plate motion data from the reconstruction is imposed as surface boundary conditions in the time-dependent model and the bottom boundary is free to slip. The temperature profile of the oceanic lithosphere follows a modified error function<sup>51</sup> following the seafloor age from the reconstruction so that the slab buoyancy is the same as that in the actual Earth, while the continental lithosphere initiates with a steady-state temperature profile (Fig. S1a). The CMB temperature is fixed to be 500°C higher than the ambient mantle. The viscosity of the model depends on depth, temperature, and composition.

The models adopt a layered and smoothed background viscosity profile within 4 depth ranges: 0–44 km, 44–410 km, 410–660 km, and 660–2867 km. Their background viscosities are  $10^{20} Pa \cdot s$ ,  $10^{20} Pa \cdot s$ ,

$10^{21} Pa \cdot s$  and  $3 \times 10^{22} Pa \cdot s$ , respectively, and the reference viscosity is set to be  $10^{21} Pa \cdot s$  (Fig. S1b). The temperature dependency of viscosity follows the equation:

$$\eta = \eta_0 \cdot C \cdot \exp\left(\frac{E_\eta}{T+T_\eta} - \frac{E_\eta}{T_m+T_\eta}\right) \# (5)$$

where  $\eta_0$  is the background viscosity,  $C$  is the compositional viscosity variation,  $E_\eta$  is the activation energy,  $T$ ,  $T_\eta$  and  $T_m$  are the temperature, activation temperature, and ambient mantle temperature, respectively. The variation of viscosity is  $10^{19}$ - $10^{23} Pa \cdot s$  in the time-dependent model and  $10^{18}$ - $10^{24} Pa \cdot s$  in the instantaneous free-slip models that attempt to reproduce plate motion.

We consider a total of 13 different chemical compositions in the model (Fig. S1d), represented by  $\sim$  1.8 billion tracers. The oceanic lithosphere is composed of a 7-km-thick surface layer that does not have buoyancy anomaly and only mimics the weak and lubricating plate interface near the trench during subduction, a 21-km-thick crustal layer whose buoyancy equals that of a 7-km-thick basaltic crust, and the underlying lithospheric mantle. The basaltic crust undergoes composition and density changes at 120 km depth following the basalt-to-eclogite phase transformation. The continental lithosphere consists of 2 layers of crust and 3 layers of mantle lithosphere. The crust has an average density of  $\sim 2.8 g/cm^3$ , with the lower crust being weaker than the upper crust to mitigate the effect of deformation from the imposed plate motion to deeper depths. The continental mantle lithosphere consists of a buoyant upper layer, a neutrally buoyant middle layer, and a dense lower layer relative to the ambient mantle that follows recent inferences<sup>53-55</sup>. More model information is available in recent studies using similar methods<sup>24-27</sup>.

## Generating Plate Motion

To reproduce plate motion and stress dynamically, we rerun the model using checkpoints stored at every 10 Myr. These reruns have the same mantle structures as in the sequential model but with a free-slip surface boundary condition. This way, internal mantle dynamics from slabs and plumes control the convective motion and drive deformation of the lithosphere, so that we can estimate the driving force of a given plate. Rigid rotation is removed during each rerun. We further remove the lithospheric net rotation from calculated plate motion for better comparison with observed plate motion in the NNR (no-net-rotation) frame. The mantle flow and stresses from the model with imposed plate motion are largely unchanged in the free-slip reruns, as shown in (28), validating the dynamic compatibility of the internal convection with observed surface kinematics. To achieve realistic plateness, we increase the viscosity of the lithosphere to  $10^{24} Pa \cdot s$  so that each plate moves as a coherent unit with little internal deformation. The viscosity of the oceanic asthenosphere is  $10^{18} Pa \cdot s$  and plate boundary viscosity is around  $10^{20} Pa \cdot s$ , in order to mimic the effect due to strain-rate weakening<sup>56</sup>. These adjusted shallow viscosity features are not effectively constrained in the sequential simulation when imposed surface kinematics override the dynamics of these features. However, a proper representation of them in the free-slip reruns is crucial given their high sensitivity to plate motion and mantle dynamics.

## Quantification of Mantle Drag and Boundary Resistance

Mantle drag is a combination of friction drag and pressure drag. Friction drag is essentially the shear stress applied near the bottom of the lithosphere due to asthenospheric flow. The friction drag along plate motion direction follows the form:

$$F_f = - \iint \frac{\tau_{r\theta}v_{p\theta} + \tau_{r\varphi}v_{p\varphi}}{|\vec{v}_p|} dA \# (6)$$

where  $F_f$  is friction drag,  $\vec{v}_p$  is plate motion velocity,  $\tau$  is the stress,  $r$ ,  $\theta$ , and  $\varphi$  are the radial, colatitudinal, and longitudinal direction, respectively, and  $A$  is the horizontal area. This value is positive for driving the plate motion and negative for resisting the plate motion. The stress used here is the maximum absolute value over depths near a viscosity-defined LAB (viscosity 10 times that of the background viscosity), from 0.75 times of this depth to 410 km.

Pressure drag is due to the blocking of horizontal mantle flow by the lithospheric step. This reflects the pressure gradient acting on the lithospheric step. Thus, computing pressure drag requires a 3D integration of the pressure gradient over the lithospheric step direction as:

$$F_p = \iiint \frac{\omega(\vec{v}_p \cdot \vec{n})(\nabla P \cdot \vec{n})}{|\vec{v}_p|} dV \# (7)$$

where  $F_p$  is pressure drag,  $\omega$  is a weighting function from the lithospheric step,  $\vec{n}$  is the lithospheric step normal vector (pointing to the lithospheric interior) and  $V$  is the volume of interest. Again, the positive value represents a driving force and vice versa. Before computing the integration, the algorithm goes through each depth of interest to find the distribution of the lithosphere (set as 1) and asthenosphere (set as 0) horizontally and acquire its gradient map (the lithospheric step).  $\vec{n}$  is the gradient unit vector and  $\omega$  is the scalar field of gradient amplitude normalized by the maximum value in the region of interest, ranging from 0 to 1.

During the calculation of plate driving force, we neglect the area within 300 km from the plate boundary to avoid potential boundary effect. For comparison to traditional estimation of slab pull and ridge push, all the mantle drag forces (in the unit of  $N$ ) are divided by the square root of plate area in each time to give the unit of  $N/m$ .

Plate boundary resistant force is computed similar to pressure drag. The northern resistant force reveals as a dynamic pressure increase towards the Indo-Eurasia collision zone. Thus, we track the pressure force within 300km and above a given latitude from the plate boundary to quantify northern boundary resistant force. The resistant force has different sign compared to driving force when projected to plate motion.

## Anisotropy Calculation

We simulate the flow-induced seismic anisotropy based on the FORTRAN code DRexS<sup>57</sup> that considers the effect of dislocation creep, dynamic recrystallization, and grain boundary migration, similar to

previous works<sup>26,57,58</sup>. The simulation initializes with randomly oriented mantle mineral aggregate that assumes 70% A-type olivine and 30% enstatite. These mineral aggregates advect and realign following the mantle flow from 20 Ma to the present day based on the free-slip models. This produces the full elastic tensors of the aggregates and, since the upper mantle is dominated by transverse isotropy, we use the symmetry axis of the transverse isotropy (TI axis) to represent the lattice-preferred orientation<sup>59</sup>.

## Declarations

**Acknowledgments:** This work is supported by National Science Foundation (NSF) grant EAR1554554. We also acknowledge the Texas Advanced Computing Center (TACC) for providing an allocation on Frontera.

**Author contributions:** Y.L. and L.L. conceptualized the idea, drafted and reviewed the manuscript, Y.L. performed the main investigation and visualization. L.L. acquired funding and supervised the project. All the authors contributed to the methodology, analysis, and interpretation.

**Competing interests:** Authors declare that they have no competing interests.

**Data and materials availability:** Most figures are prepared with GMT (<https://www.generic-mapping-tools.org/>) and Paraview (<https://www.paraview.org/>). Surface velocity and plate boundary files are exported using Gplates (<https://www.gplates.org/>). The original version of CitcomS is available at [www.geodynamics.org/cig/software/citcoms/](http://www.geodynamics.org/cig/software/citcoms/). The seismic tomography and anisotropy models are available in their respective references. All data in this research will be available online.

## References

1. S. Zahirovic, R. D. Müller, M. Seton, N. Flament, M. Gurnis, J. Whittaker, Insights on the kinematics of the India-Eurasia collision from global geodynamic models. *Geochemistry, Geophysics, Geosystems*. 13 (2012), doi:10.1029/2011GC003883.
2. R. D. Müller, M. Seton, S. Zahirovic, S. E. Williams, K. J. Matthews, N. M. Wright, G. E. Shephard, K. T. Maloney, N. Barnett-Moore, M. Hosseinpour, D. J. Bower, J. Cannon, Ocean Basin Evolution and Global-Scale Plate Reorganization Events Since Pangea Breakup. *Annu Rev Earth Planet Sci*. 44, 107–138 (2016).
3. Y. Niu, What drives the continued India-Asia convergence since the collision at 55 Ma? *Sci Bull*. 65 (2020), pp. 169–172.
4. P. Molnar, P. England, J. Martinod, Mantle dynamics, uplift of the Tibetan Plateau, and the Indian Monsoon. *Reviews of Geophysics*. 31 (1993), pp. 357–396.
5. A. Ghosh, W. E. Holt, L. M. Flesch, A. J. Haines, Gravitational potential energy of the Tibetan Plateau and the forces driving the Indian plate. *Geology*. 34, 321–324 (2006).
6. A. Copley, J. P. Avouac, J. Y. Royer, India-Asia collision and the Cenozoic slowdown of the Indian plate: Implications for the forces driving plate motions. *J Geophys Res Solid Earth*. 115 (2010),

doi:10.1029/2009JB006634.

7. D. Forsyth, S. Uyedaf, On the Relative Importance of the Driving Forces of Plate Motion. *Geophysical Journal of the Royal Astronomical Society*. 43, 163–200 (1975).
8. D. L. Turcotte, G. Schubert, *Geodynamics*. (Cambridge University Press, 2002).
9. C. Li, R. D. van der Hilst, E. R. Engdahl, S. Burdick, A new global model for P wave speed variations in Earth's mantle. *Geochemistry, Geophysics, Geosystems*. 9 (2008), doi:10.1029/2007GC001806.
10. M. Amaru, *Global travel time tomography with 3-D reference models*. Utrecht University, Vol. 274, (2007).
11. R. D. Müller, S. Zahirovic, S. E. Williams, J. Cannon, M. Seton, D. J. Bower, M. G. Tetley, C. Heine, E. le Breton, S. Liu, S. H. J. Russell, T. Yang, J. Leonard, M. Gurnis, A Global Plate Model Including Lithospheric Deformation Along Major Rifts and Orogens Since the Triassic. *Tectonics*. 38, 1884–1907 (2019).
12. T. H. Torsvik, B. Steinberger, G. E. Shephard, P. V. Doubrovine, C. Gaina, M. Domeier, C. P. Conrad, W. W. Sager, Pacific-Panthalassic Reconstructions: Overview, Errata and the Way Forward. *Geochemistry, Geophysics, Geosystems*. 20, 3659–3689 (2019).
13. F. A. Capitanio, G. Morra, S. Goes, R. F. Weinberg, L. Moresi, India-Asia convergence driven by the subduction of the Greater Indian continent. *Nat Geosci*. 3, 136–139 (2010).
14. Y. Wang, L. Zhang, Z. H. Li, Metamorphic densification can account for the missing felsic crust of the Greater Indian continent. *Commun Earth Environ*. 3, 166 (2022).
15. L. Chen, F. A. Capitanio, L. Liu, T. v. Gerya, Crustal rheology controls on the Tibetan plateau formation during India-Asia convergence. *Nat Commun*. 8 (2017), doi:10.1038/ncomms15992.
16. J. Li, X. Song, Tearing of Indian mantle lithosphere from high-resolution seismic images and its implications for lithosphere coupling in southern Tibet. *Proc Natl Acad Sci U S A*. 115, 8296–8300 (2018).
17. G. Stadler, M. Gurnis, C. Burstedde, L. C. Wilcox, L. Aliscic, O. Ghattas, The Dynamics of Plate Tectonics and Mantle Flow: From Local to Global Scales. *Science*. 329, 1033–1038 (2010).
18. F. A. Capitanio, Current deformation in the Tibetan Plateau: A stress gauge in the India-Asia collision tectonics. *Geochemistry, Geophysics, Geosystems*, 21, e2019GC008649 (2020), doi:10.1029/2019GC008649
19. S. Bose, W. P. Schellart, V. Strak, J. C. Duarte, Z. Chen, Sunda subduction drives ongoing India-Asia convergence. *Tectonophysics*, 849 (2023), doi:10.1016/j.tecto.2023.229727
20. X. Zhou, Z. H. Li, T. v. Gerya, R. J. Stern, Lateral propagation–induced subduction initiation at passive continental margins controlled by preexisting lithospheric weakness. *Sci Adv*. 6 (2020), doi:10.1126/sciadv.aaz1048.
21. N. Coltice, L. Husson, C. Faccenna, M. Arnould, What drives tectonic plates? *Sci Adv*. 5, eaax4295 (2019).

22. C. P. Conrad, C. Lithgow-Bertelloni, The temporal evolution of plate driving forces: Importance of “slab suction” versus “slab pull” during the Cenozoic. *J Geophys Res Solid Earth*. 109 (2004), doi:10.1029/2004JB002991.
23. T. W. Becker, C. Faccenna, Mantle conveyor beneath the Tethyan collisional belt. *Earth Planet Sci Lett*. 310, 453–461 (2011).
24. D. Peng, L. Liu, Quantifying slab sinking rates using global geodynamic models with data-assimilation. *Earth Sci Rev*. 230 (2022), doi:10.1016/j.earscirev.2022.104039.
25. D. Peng, L. Liu, Y. Wang, A Newly Discovered Late-Cretaceous East Asian Flat Slab Explains Its Unique Lithospheric Structure and Tectonics. *J Geophys Res Solid Earth*. 126 (2021), doi:10.1029/2021JB022103.
26. D. Peng, L. Liu, J. Hu, S. Li, Y. Liu, Formation of East Asian Stagnant Slabs Due To a Pressure-Driven Cenozoic Mantle Wind Following Mesozoic Subduction. *Geophys Res Lett*. 48 (2021), doi:10.1029/2021GL094638.
27. Y. Li, L. Liu, D. Peng, H. Dong, S. Li, Evaluating tomotectonic plate reconstructions using geodynamic models with data assimilation, the case for North America. *Earth Sci Rev*. 244 (2023), doi: 10.1016/j.earscirev.2023.104518
28. Y. Liu, L. Liu, Y. Li, D. Peng, Z. Wu, Z. Cao, S. Li, Q. Du, Global back-arc extension due to trench-parallel mid-ocean ridge subduction. *Earth Planet Sci Lett*. 600 (2022), doi:10.1016/j.epsl.2022.117889.
29. Z. Cao, L. Liu, Origin of Three-Dimensional Crustal Stress Over the Conterminous United States. *J Geophys Res Solid Earth*. 126 (2021), doi:10.1029/2021JB022137.
30. W. Mao, S. Zhong, Constraints on Mantle Viscosity From Intermediate-Wavelength Geoid Anomalies in Mantle Convection Models With Plate Motion History. *J Geophys Res Solid Earth*. 126 (2021), doi:10.1029/2020JB021561.
31. K. Yuan, C. Beghein, Seismic anisotropy changes across upper mantle phase transitions. *Earth Planet Sci Lett*. 374, 132–144 (2013).
32. L. Liu, M. Gurnis, Simultaneous inversion of mantle properties and initial conditions using an adjoint of mantle convection. *J Geophys Res Solid Earth*. 113 (2008), doi:10.1029/2008jb005594.
33. L. Chen, X. Wang, X. Liang, B. Wan, L. Liu, Subduction tectonics vs. Plume tectonics—Discussion on driving forces for plate motion. *Sci China Earth Sci*. 63 (2020), pp. 315–328.
34. A. Ghosh, W. E. Holt, Plate motions and stresses from global dynamic models. *Science*. 335, 838–843 (2012).
35. X. Zhong, Z. H. Li, Wedge-Shaped Southern Indian Continental Margin Without Proper Weakness Hinders Subduction Initiation. *Geochemistry, Geophysics, Geosystems*. 23 (2022), doi:10.1029/2021GC009998.
36. C. P. Conrad, C. Lithgow-Bertelloni, Influence of continental roots and asthenosphere on plate-mantle coupling. *Geophys Res Lett*. 33 (2006), doi:10.1029/2005GL025621.

37. M. L. Rudolph, S. J. Zhong, History and dynamics of net rotation of the mantle and lithosphere. *Geochemistry, Geophysics, Geosystems*. 15, 3645–3657 (2014).
38. J. Paul, C. P. Conrad, T.W. Becker, & A. Ghosh, Convective self-compression of cratons and the stabilization of old lithosphere. *Geophysical Research Letters*, 50, e2022GL101842 (2023), doi:10.1029/2022GL101842
39. M. D. Wamba, J. P. Montagner, B. Romanowicz, Imaging deep-mantle plumbing beneath La Réunion and Comores hot spots: Vertical plume conduits and horizontal ponding zones. *Sci Adv*. 9 (2023), doi:10.1126/sciadv.ade3723.
40. D. J. J. van Hinsbergen, B. Steinberger, P. v. Doubrovine, R. Gassmöller, Acceleration and deceleration of India-Asia convergence since the Cretaceous: Roles of mantle plumes and continental collision. *J Geophys Res Solid Earth*. 116 (2011), doi:10.1029/2010JB008051.
41. S. C. Cande, D. R. Stegman, Indian and African plate motions driven by the push force of the Réunion plume head. *Nature*. 475, 47–52 (2011).
42. O. Jagoutz, L. Royden, A. F. Holt, T. W. Becker, Anomalously fast convergence of India and Eurasia caused by double subduction. *Nat Geosci*. 8, 475–478 (2015).
43. P. Kumar, X. Yuan, M. R. Kumar, R. Kind, X. Li, R. K. Chadha, The rapid drift of the Indian tectonic plate. *Nat Commun*. 449, 894–897 (2007).
44. W. Wang, P. A. Cawood, M. K. Pandit, J. H. Zhao, J. P. Zheng, No collision between Eastern and Western Gondwana at their northern extent. *Geology*. 47, 308–312 (2019).
45. S. Liu, S. D. King, Dynamics of the North American Plate: Large-Scale Driving Mechanism From Far-Field Slabs and the Interpretation of Shallow Negative Seismic Anomalies. *Geochemistry, Geophysics, Geosystems*. 23 (2022), doi:10.1029/2021GC009808.
46. B. Wan, F. Wu, L. Chen, L. Zhao, X. Liang, W. Xiao, R. Zhu, Cyclical one-way continental rupture-drift in the Tethyan evolution: Subduction-driven plate tectonics. *Sci China Earth Sci*. 62 (2019), pp. 2005–2016.
47. Z. X. Li, R. N. Mitchell, C. J. Spencer, R. Ernst, S. Pisarevsky, U. Kirscher, J. B. Murphy, Decoding Earth's rhythms: Modulation of supercontinent cycles by longer superocean episodes. *Precambrian Res*. 323, 1–5 (2019).
48. S. Zhong, N. Zhang, Z. X. Li, J. H. Roberts, Supercontinent cycles, true polar wander, and very long-wavelength mantle convection. *Earth Planet Sci Lett*. 261, 551–564 (2007).
49. S. Zhong, M. T. Zuber, L. Moresi, M. Gurnis, Role of temperature-dependent viscosity and surface plates in spherical shell models of mantle convection. *J Geophys Res Solid Earth*. 105, 11063–11082 (2000).
50. J. Hu, L. Liu, Abnormal seismological and magmatic processes controlled by the tearing South American flat slabs. *Earth Planet Sci Lett*. 450, 40–51 (2016).
51. L. Liu, D. R. Stegman, Segmentation of the Farallon slab. *Earth Planet Sci Lett*. 311, 1–10 (2011).

52. J. Hu, L. Liu, M. Faccenda, Q. Zhou, K. M. Fischer, S. Marshak, C. Lundstrom, Modification of the Western Gondwana craton by plume-lithosphere interaction. *Nat Geosci.* 11, 203–210 (2018).
53. Q. Zhou, L. Liu, J. Hu, Western US volcanism due to intruding oceanic mantle driven by ancient Farallon slabs. *Nat Geosci.* 11, 70–76 (2018).
54. Y. Wang, L. Liu, Q. Zhou, Geoid Reveals the Density Structure of Cratonic Lithosphere. *J Geophys Res Solid Earth.* 127 (2022), doi:10.1029/2022JB024270.
55. Y. Wang, L. Liu, Q. Zhou, Topography and Gravity Reveal Denser Cratonic Lithospheric Mantle Than Previously Thought. *Geophys Res Lett.* 49 (2022), doi:10.1029/2021GL096844.
56. J. Hu, L. Liu, M. Gurnis, Southward expanding plate coupling due to variation in sediment subduction as a cause of Andean growth. *Nat Commun.* 12 (2021), doi:10.1038/s41467-021-27518-8.
57. J. Hu, M. Faccenda, L. Liu, Subduction-controlled mantle flow and seismic anisotropy in South America. *Earth Planet Sci Lett.* 470, 13–24 (2017).
58. Q. Zhou, J. Hu, L. Liu, T. Chaparro, D. R. Stegman, M. Faccenda, Western U.S. seismic anisotropy revealing complex mantle dynamics. *Earth Planet Sci Lett.* 500, 156–167 (2018).
59. M. Faccenda, F. A. Capitanio, Seismic anisotropy around subduction zones: Insights from three-dimensional modeling of upper mantle deformation and SKS splitting calculations. *Geochemistry, Geophysics, Geosystems.* 14, 243–262 (2013).

## Figures



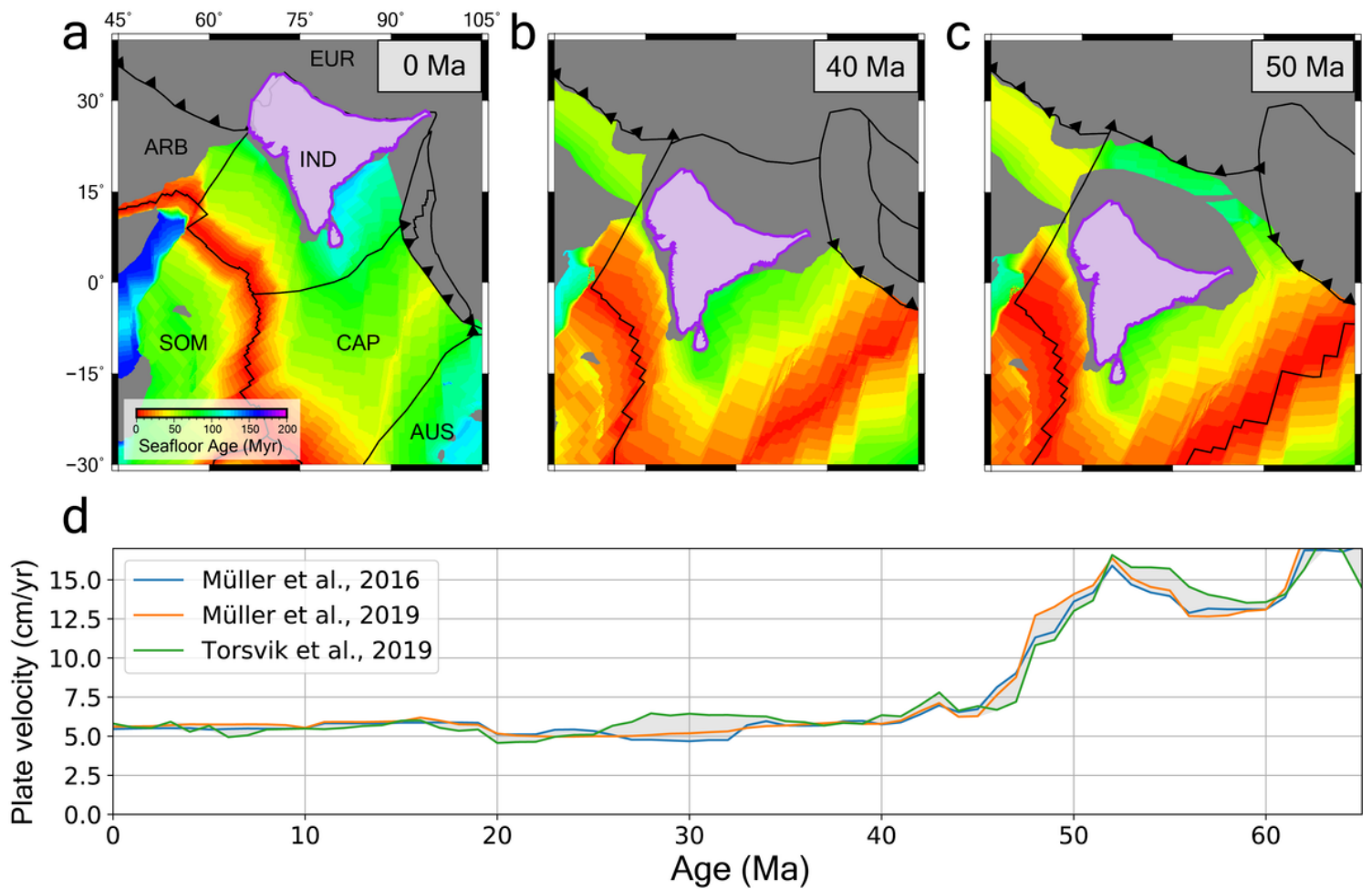


**Figure 1**

**Cenozoic Indian configuration and plate motion.** (a-c) Plate reconstruction at 0, 40, and 50 Ma, respectively<sup>2</sup> showing the history of continent-continent collision. ARB: Arabian plate, AUS: Australian plate, CAP: Capricorn plate, EUR: Eurasian plate, IND: Indian plate, SOM: Somalian plate. (d) Cenozoic Indian plate speed in the no-net-rotation frame (NNR) from three different reconstructions<sup>2,11,12</sup>.

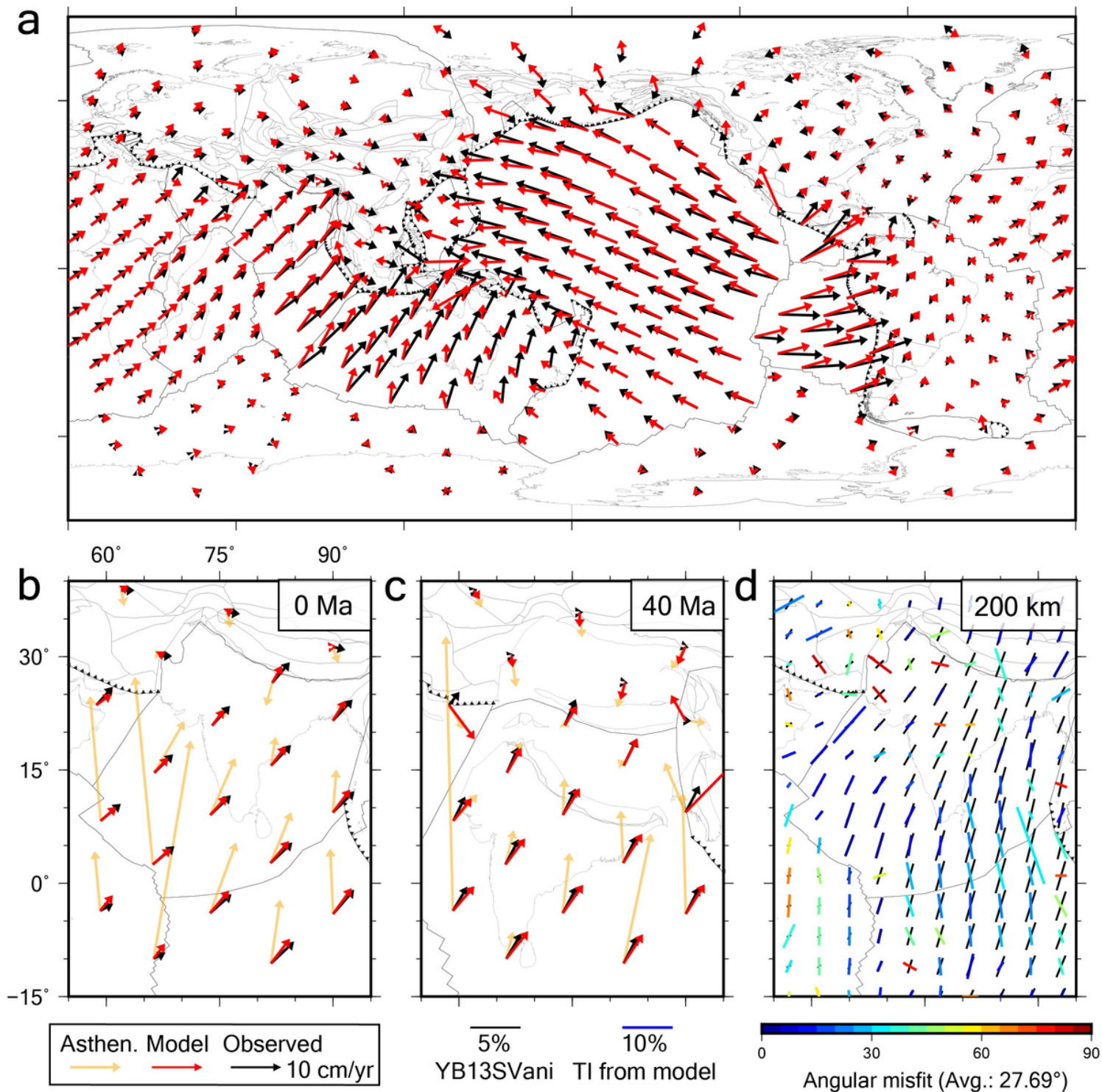
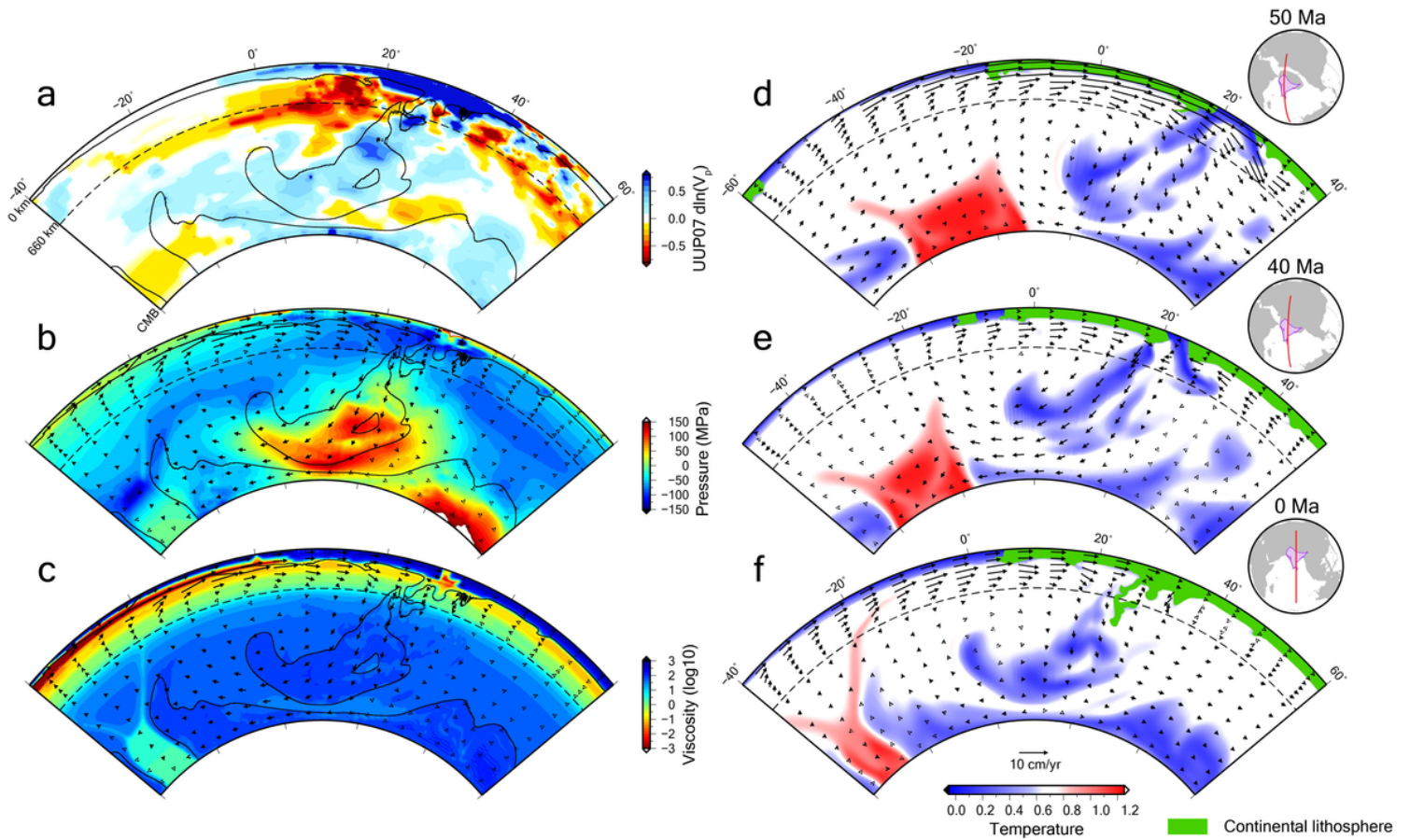


Figure 2

**Plate motion, asthenospheric flow, and anisotropy comparison.** (a-c) Comparison between modeled plate motion and that from the reconstruction<sup>2</sup>, as well as asthenospheric flow in **b** and **c**. The shown asthenospheric flow is the maximum upper-mantle velocity below the lithosphere. (d) Comparison between modeled and observed anisotropy, based on the model YB13SVani<sup>31</sup>. TI represents the symmetry axis of the transverse isotropy.



**Figure 3**

**Neo-Tethyan slab evolution and viscosity, dynamic pressure in model and tomography.** (a) Comparison between the tomography UUP07<sup>10</sup> and modeled slab structure (dark contour denotes the 0.45 temperature volume). (b) Modeled dynamic pressure at 0Ma. (c) Modeled viscosity structure at 0Ma. (d-f) Modeled mantle evolution tracking the Indian collision process with mantle velocity.



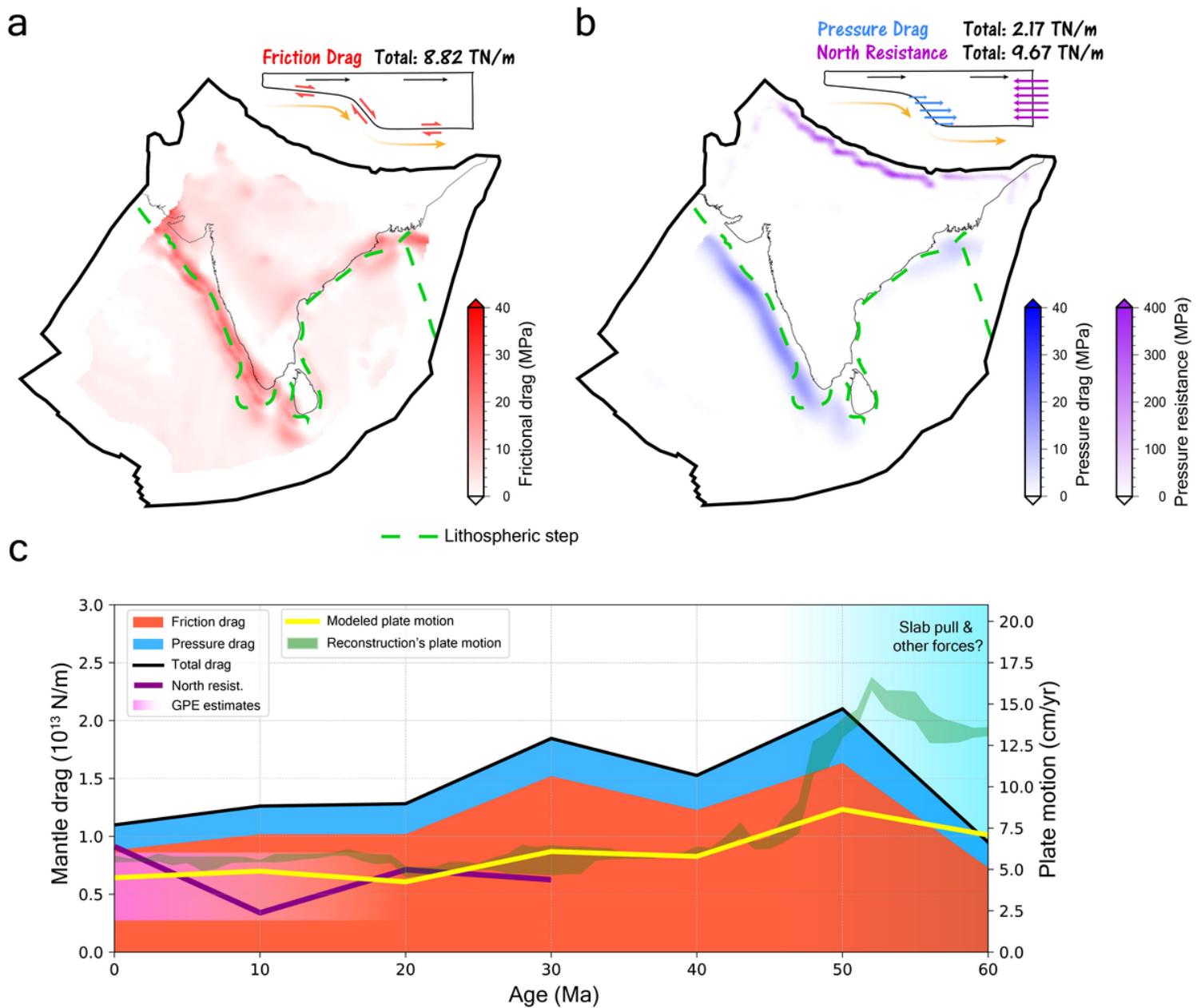


**Figure 4**

**Quantification of two types of mantle drag and their evolution.** (a) Friction drag schematic and its modeled distribution within the Indian plate. (b) Pressure drag and northern boundary resistance schematics and their modeled distributions within the Indian plate. A unit of force per area is chosen for better comparison to friction drag. Note the scale difference between drag and resistant force. Both friction drag and pressure drag are projected to the plate motion direction. (c) Evolution of modeled mantle drag (colored areas), northern Indian boundary resistance, observed (from Fig. 1d) vs predicted plate motion history during the Cenozoic (line features). Since the Tethyan slab detaches between 30-40Ma, we quantify northern resistance only from 30Ma. The gradational light blue region prior to 45 Ma represents other potential driving forces not considered in our model.

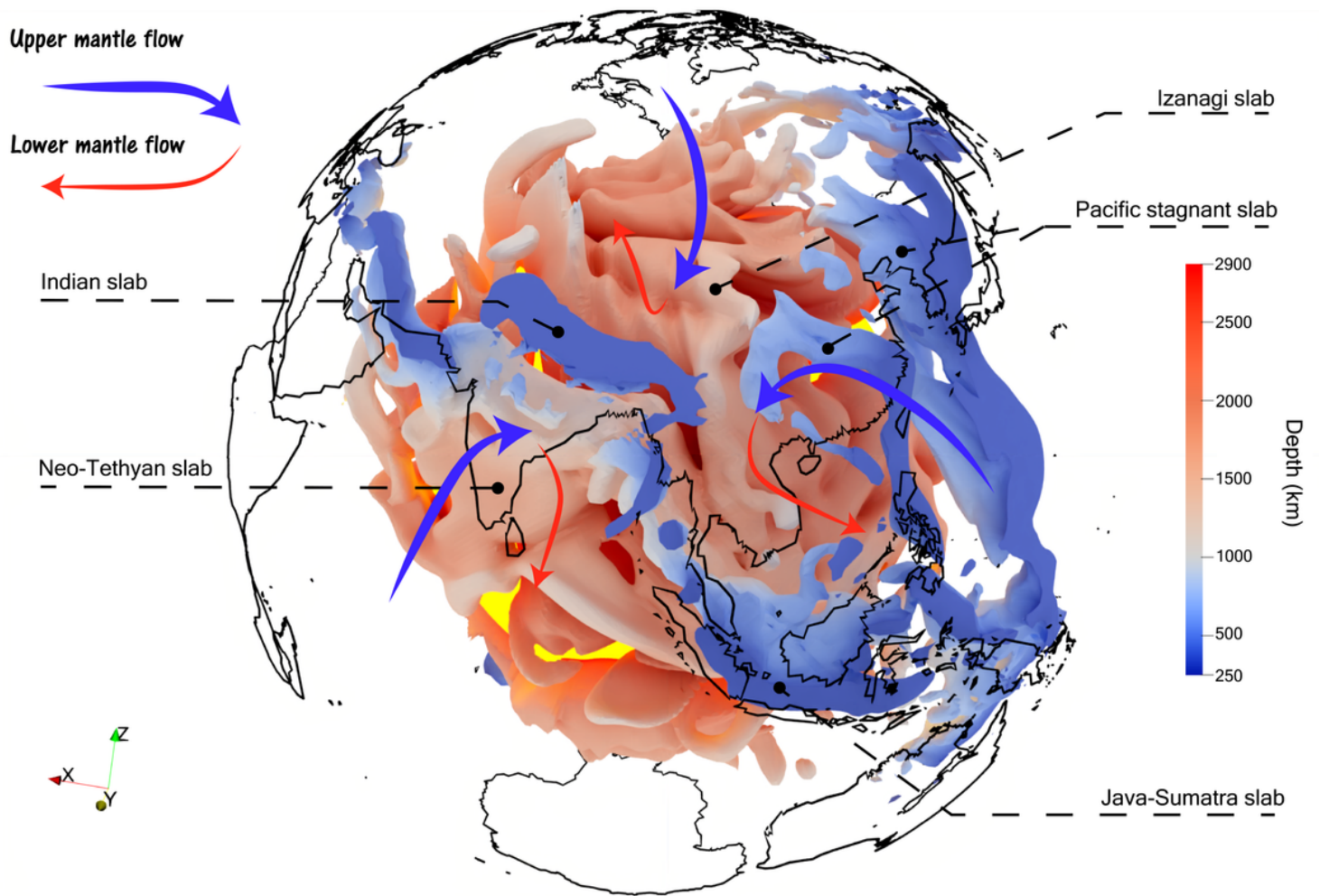


**Figure 5**

**Modeled East Asian slabs and hemispheric converging flow.** The blue-to-red volumes are present-day slabs with a temperature 150 °C lower than the ambient mantle at >250 km depth. Arrowed curves indicate the pattern of depth-dependent mantle flow from three different directions corresponding to three subduction zones. All major slabs are annotated. See movie S2 for 3D streamlines and the velocity field.

## Supplementary Files

This is a list of supplementary files associated with this preprint. Click to download.

- [MovieS1.mp4](#)
- [MovieS2.mp4](#)
- [supplementaryIndianOceanNCsubmit.docx](#)